Understanding the Origin of Structure Sensitivity in Hydrodechlorination of Trichloroethylene on Palladium Catalyst

Understanding the Origin of Structure Sensitivity in Hydrodechlorination of Trichloroethylene on Palladium Catalyst

Chaitra S. Shenoy[a], Tuhin S. Khan[b]*, Kirti Verma[a], Mesfin Tsige[c], Kshitij C. Jha[c,d,e], M. Ali Haider[a]*, Shelaka Gupta[f]*

[a] Renewable Energy and Chemicals Laboratory, Department of Chemical Engineering, Indian Institute of Technology Delhi, Hauz Khas, New Delhi 110016, India

[b] Light Stock Processing Division, CSIR - Indian Institute of Petroleum, Mohkampur, Dehradun 248005, India

[c] College of Polymer Science and Polymer Engineering, The University of Akron, Akron, Ohio 44325, United States

[d] Biena Tech LLC, 526 S Main St, Akron, Ohio 44311, United States

[e] Department of Chemical Engineering, Indian Institute of Technology Delhi, Hauz Khas, New Delhi 110016, India

[f] Department of Chemical Engineering, Indian Institute of Technology Hyderabad, Kandi, Sangareddy, Telangana 502285, India

* Corresponding Authors: Tuhin S. Khan (tuhins.khan@iip.res.in), M. Ali Haider (haider@iitd.ac.in), Shelaka Gupta (shelaka@che.iith.ac.in)

Keywords:

Density functional theory, Hydrodechlorination, Trichloroethylene, Pd Catalyst, Water pollutant

Abstract

Periodic density functional theory (DFT) calculations are employed to understand the origin of structure sensitivity in hydrodechlorination (HDC) of trichloroethylene (TCE) over different facets of a palladium catalyst. The HDC reaction is simulated on the terrace (Pd (111) and Pd (100)) and undercoordinated (Pd (211) and Pd (110)) sites of the Pd catalyst. The most stable binding configuration of TCE on the Pd surfaces is observed to be through the di-σ mode of binding, wherein each carbon atom of the TCE molecule is adsorbed atop of the Pd atom. On comparing TCE adsorption over different facets of Pd, a maximum binding energy of -178 kJ/mol is calculated over the Pd (110) surface. TCE, upon adsorption on Pd catalyst, undergoes dechlorination followed by hydrogenation of the hydrocarbon intermediates. The activation energies for C-Cl bond

dissociation steps are significantly low when compared to the hydrogenation steps. The chlorine released from dechlorination tends to block the active sites, thereby poisoning the surface with high binding energies (B.E > -160 kJ/mol) on all the surfaces. The trend in chlorine binding energies on Pd facets follows: Pd (110) > Pd (211) > Pd (100) > Pd (111). The removal of surface chlorine is facilitated by its reaction with surface hydrogen to form hydrogen chloride. The activation energy for hydrogen chloride formation is calculated to be 90 kJ/mol and 88 kJ/mol on Pd (111) and Pd (100) terrace sites, respectively and 109 kJ/mol and 118 kJ/mol on the stepped Pd (211) and corrugated Pd (110) facets, respectively. This suggests the ease of removal of Cl as HCl from the terrace sites as compared to the step and corrugated sites. The structure sensitivity in the TCE HDC reaction could possibly arise due to the differences in the energetics of Cl removal on different Pd facets. This mechanistic understanding could provide a rationale for designing suitable catalysts for the HDC of TCE.

Introduction

The extensive use of trichloroethylene (TCE) as a solvent in industries has led to groundwater contamination, thus affecting a major source of drinking water for the global population. As TCE does not degrade naturally, it lingers in groundwater, with adverse consequences for human health[1,2]. According to the guidelines established by World Health Organization, the permissible limit of TCE in drinking water is 0.02 ppm[3], which is quite low in comparison to its solubility limit in water (1100 ppm)[4]. Catalytic treatment in the presence of hydrogen, also known as the hydrodechlorination (HDC) is an effective technique for removal of trace amounts of this contaminant from groundwater. This remediation technique is found to be economically feasible, when compared with competing technologies (such as air stripping, granular activated carbon (GAC) adsorption and permeable reactive barrier (PRB))[5]. To aid the conversion of TCE to non-chlorinated products, transition metals are used as catalysts. For instance, Kovenklioglu and co-workers conducted aqueous phase HDC experiments, catalyzed by transition metals (Pd, Pt and Rh) at ambient temperature and pressure conditions, for removal of chlorinated hydrocarbons[6]. They reported 90% conversion for Pd supported on carbon (Pd/C) within 3 hours, with no detectable derived chlorinated compounds[6]. Similarly, Schreier and Reinhard observed Pd to be more effective (in comparison to Pt, Rh and Ni) for the aqueous phase transformation of

chlorinated ethylene compounds (tetrachloroethylene, TCE, cis-dichloroethylene, trans-dichloroethylene and vinyl chloride) leading to formation of ethane as the major product[7].

The ability of Pd to dissociate hydrogen and convert TCE to harmless compounds with minimal by-product formation (lesser chlorinated compounds) makes it suitable for use as a HDC catalyst[8–10]. However, Pd is still susceptible to poisoning due to Cl released during the reaction. This tendency has been studied by Ordonez et al. for treating TCE present in wastewater, catalyzed by supported Pd metal[11]. Similarly, the deactivating effect of Cl has also been reported in an experimental study by Heck and co-workers[12], on Pd nanoparticles and Pd/Al$_2$O$_3$ catalyst, resulting in decrease in the turnover frequency (TOF). The surface Cl combines with H to form byproduct HCl. Using density functional theory (DFT) calculations, Andersin et al. noted that the removal of adsorbed Cl atom as HCl in the aqueous phase was easier than moving it to the gas-phase[13]. This is also supported by temperature programmed desorption (TPD) experiments, where HCl is observed to form as a result of combinative desorption of Cl and H on the Pd (111) surface, in the process of fragmentation of cis-1,2-dichloroethene[14].

Similar to ethylene, TCE is generally adsorbed on the Pd surface through the carbon atom[15–17]. In the HDC reaction on the Pd catalyst, TCE is suggested to undergo C-Cl bond dissociation (complete dechlorination), followed by the C-H bond formation (hydrogenation of the hydrocarbon intermediates) on Pd (111) surface[13,18]. TCE HDC is postulated to follow Langmuir Hinshelwood mechanism (wherein all the adsorbates bind to the surface prior to the reaction)[19], therefore, the catalyst surface and hence, the coordination number of surface atoms can play an integral role in determining the activity and selectivity[20–23]. This can also be correlated with the particle size of the catalyst and adsorption strength of reaction intermediates. To elaborate on the same, model calculations performed by Bond showed that an increase in the particle size from 2 nm to 10 nm led to the decrease in the number of surface atoms exposed (dispersion) and increase in the coordination number of the surface atoms[24]. On exposing different Pd facets by varying its shape and size, a significant difference in the catalytic activity (in terms of TOF) is measured for the removal of nitrite, N-nitroso dimethylamine and diatrizoate from water[25]. Therefore, the reaction is suggested to be structure sensitive with a correlation to the distribution of facets. Similarly, for the aqueous phase HDC of TCE, a particle size effect is observed by Diaz and co-workers[4].

Using DFT simulations, Andersin et al. have reported the mechanism of TCE HDC over the majority Pd (111) and Pd supported on Au (111) surface[13]. Similarly, theoretical study on different Pd surfaces, for understanding the mechanism of HDC of chloroform and the poisoning effect of Cl has been reported by Xu and co-workers[26]. In this work, DFT simulations are carried out over different Pd facets, so as to develop mechanistic insights for the HDC reaction of TCE. In order to accomplish this, HDC of TCE is studied on four different Pd facets: Pd (111), Pd (211), Pd (100) and Pd (110)[27,28]. The reaction energetics are interpreted to underline the origin of structure-sensitivity in the HDC reaction of TCE over the Pd catalyst.

Methodology:

Periodic DFT calculations are performed using Vienna ab initio Simulation Package (VASP 5.3.5)[29] as employed by our group in prior studies[30,31]. The unit cell size for different Pd facets is considered such that it accommodates the adsorbates, with negligible lateral interaction. Thus, the Pd (111), Pd (100) and Pd (110) surfaces are modelled using a 4x4 supercell whereas the Pd (211) surface is modelled using a 2x4 supercell. Each periodic slab consists of four Pd atomic layers, where the bottom two layers are fixed to mimic the bulk and the top two layers are allowed to relax with the adsorbates. A vacuum slab of 20 Å is introduced to model surface reactions. The Kohn Sham equations are solved by employing the generalized gradient approximation (GGA) - Revised Perdew-Burke-Ernzerhof (RPBE) exchange-correlation functional[32]. The frozen core approximation as incorporated in Ultrasoft Pseudopotentials (USPP)[33] is used to optimize the electronic structures and the plane wave basis sets are expanded to an energy cutoff value of 396 eV. To incorporate the dispersion corrections proposed by Grimme et al.[34], DFT-D3 method is used. The first Brillouin zone is sampled using a 3x3x1 Monkhorst-Pack k-point mesh[35]. For all structural optimizations, the energy convergence criteria is set to 1×10^{-6} eV and the force convergence value is set to 0.05 eV/Å. The binding energies of adsorbates and intermediates are calculated as follows:

Binding Energy (B.E) = $E_{total} - E_{surface} - E_{adsorbate(g)}$

where, the E_{total} represents the total energy of Pd slab and adsorbate on the surface, $E_{surface}$ represents the energy of the cleaved Pd metal surface and $E_{adsorbate(g)}$ represents the energy of the adsorbate in the gas-phase.

Transition state (TS) structures on the minimum energy path (MEP) connecting the reactant and product state structures by linear interpolations are predicted by the Nudged Elastic Band (NEB)[36] algorithm in the framework of the VASP code. An improvised version of the NEB code implementing the Climbing Image - Nudged Elastic Band (CI-NEB)[37] algorithm is applied to locate the TS structure corresponding to one imaginary frequency along the reaction coordinate. A set of 8 images are given between the optimized reactant and product state geometries. The forces on each structure along the MEP is converged to a value of 0.1 eV/Å. The activation energy and reaction energy are calculated as follows:

Activation Energy $(E_a) = E_{transition\ state} - E_{reactant\ state}$

Reaction Energy $(E_{rxn}) = E_{product\ state} - E_{reactant\ state}$

where, the $E_{transition\ state}$, $E_{reactant\ state}$ and $E_{product\ state}$ represent the energy of the transition state, reactant state, and product state structures, respectively.

Results and Discussion:

Late transition metal catalysts such as Rh[38], Ru[39], Pd[40,41], Pt[42] have been widely used for HDC of TCE. Out of these, Pd has been proposed as the best catalyst based on its high conversion and selectivity towards non-chlorinated compounds at ambient temperature and atmospheric pressure conditions for the HDC reaction[43,44]. During the experiments, no chlorinated compounds are observed as reaction intermediates in the presence of a Pd catalyst. Based on this information, it is inferred that HDC reaction occurs via successive dechlorination steps followed by hydrogenation (direct route), wherein complete dechlorination occurs first with no hydrogen addition step or desorption of the derived chlorinated intermediates. By utilizing DFT simulations, Andersin and co-workers explored this pathway (Scheme 1) for the HDC of TCE on Pd (111) surface[13]. The detailed mechanistic routes for HDC of TCE are shown in Figure S1. The results obtained in the above study are in agreement with the kinetic Monte Carlo simulations performed by Kausamo et al.[18]. These studies confirm the direct pathway to be favored over other routes of HDC owing to lower activation energies for the dechlorination steps on Pd (111) surface. Since smaller particles contain a higher fraction of step and kink sites (undercoordinated sites) compared to the terrace sites[24,45–47], the change in the reactivity trends can be attributed to the change in the type of these

sites. In the present study, an attempt is made to understand the role of different facets of a Pd nanoparticle for HDC of TCE.
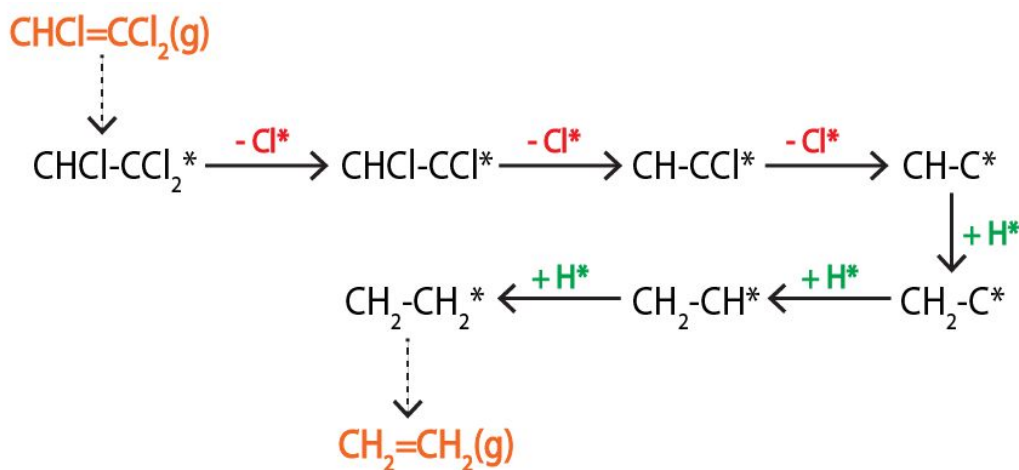
Scheme 1. The proposed mechanistic route for the HDC of TCE over Pd surface as suggested in reference [13] ((g) represents gas-phase species and superscript * denotes adsorbed species).

TCE is placed in different configurations on the Pd (111), Pd (100), Pd (211) and Pd (110) surfaces but it did not bind through chlorine which could be attributed to its high electronegativity (Figure S2 displays all the π-bound TCE configurations on Pd facets). It is observed that in the most stable binding configuration on all Pd facets, TCE prefers to bind through di-σ mode, wherein each carbon atom sits on an atop position on the Pd atom as shown in Figure 1 ((a) to (d)). Upon adsorption on different Pd facets, TCE undergoes distortion leading to stretching of the C-H, C-Cl and C-C bonds. The C-Cl bond in cis-position to C-H bond tends to undergo maximum elongation on all four facets (~0.07 Å to 0.08 Å longer in comparison with its gas-phase bond length[13], Figure 1). For TCE in the gas-phase, the C-Cl bond has a length of 1.73 Å. This value correlates well with the calculated gas-phase C-Cl bond length (in cis-position relative to C-H) obtained by Andersin et al[13]. The TCE binding energy in this configuration on Pd (111) is calculated to be -138 kJ/mol (Figure 1 (a)), which is higher than the value reported by Andersin and Honkala on Pd (111) surface (binding energy = -55 kJ/mol)[19]. This difference in the binding energy may be ascribed to the use of different pseudopotentials, exchange and correlation functionals and addition of the van der Waals interaction in this study. Similarly, the binding energy of TCE in di-σ mode is calculated

to be -149 kJ/mol on Pd (211) (Figure 1 (b)), -152 kJ/mol on Pd (100) (Figure 1 (c)) and -178 kJ/mol on Pd (110) (Figure 1 (d)). Furthermore, the order of TCE adsorption energy calculated on different Pd facets (Pd (110) > Pd (100) > Pd (211) > Pd (111)) correlates well with the position of the d-band center of these Pd surfaces with respect to the Fermi level[48]. In general, the increase in reactivity can be attributed to the decrease in the coordination number of the surface atoms of Pd.
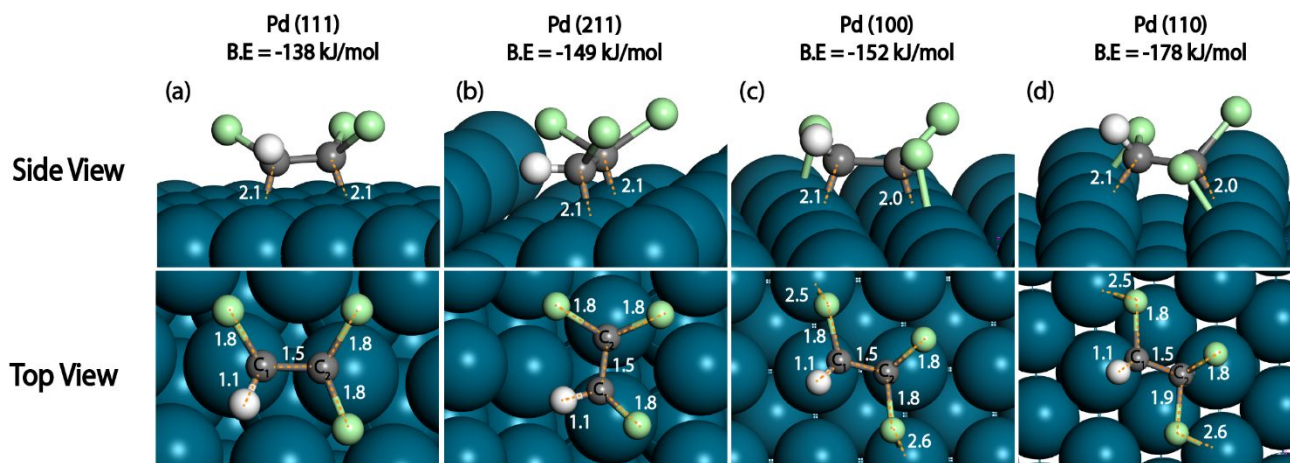

Figure 1. The most stable binding mode of TCE on (a) Pd (111), (b) Pd (211), (c) Pd (100) and (d) Pd (110) surfaces. The Pd atoms are displayed in blue, Cl atoms in green, C atoms in grey and H atom in white color. Distances are marked in Å.

Due to the stretching of C-Cl bonds upon binding to the Pd surface, dechlorination is the preferred route compared to the hydrogenation route[13]. Table S1 displays the activation energies and reaction energies for hydrogenation of TCE and the chlorinated intermediates on Pd facets. Mackenzie and co-workers explored the structure-reactivity relations of various saturated and unsaturated chlorinated contaminants. The authors reported the addition of hydrogen to chlorinated ethenes to be the rate determining step (RDS)[49], which is in agreement with our results. From our DFT study (Table S1), direct addition of a hydrogen atom to TCE results in a significantly high activation energy over all Pd facets and thus, would not be the preferred pathway. Owing to maximum bond stretch, the C-Cl bond in cis-position relative to C-H bond tends to undergo cleavage on all Pd facets. The carbon atom with one chlorine atom is marked as C_1 and the carbon having two chlorine atoms is marked as C_2 (Figure 1). Figure 2 displays the first dechlorination step over Pd (111), Pd (211), Pd (100) and Pd (110) surfaces. On Pd (111) surface, considered to be the most abundant

facet, the di-σ mode bound TCE undergoes first C-Cl bond dissociation as shown in Figure 2 (1A to 1B). This C-Cl bond has a length of 1.8 Å. At the transition state, C-Cl bond is stretched to 2.1 Å, with the Cl atom bending slightly towards the Pd surface and at a distance of 2.8 Å from the nearest Pd atom (Figure 2 (TS_{1A})). In the final state, the Cl atom breaks completely from the TCE molecule and sits at the closest hollow site of Pd (111), forming CHCl-CCl as an intermediate (Figure 2 (1B)). The activation energy for this step on Pd (111) is calculated to be 25 kJ/mol, which is close to the value reported by Andersin et al., having an activation energy of 22 kJ/mol and is exothermic (E_{rxn} = -104 kJ/mol)[13]. Similarly, on the Pd (211) facet, TCE is found to bind to the terrace site of the surface. The C-Cl bond undergoes bond elongation from 1.8 Å in the reactant state to 2.2 Å in the transition state and to 4.2 Å in the final state (Figure 2 (2A to 2B)). In the product state, the Cl atom binds in a bridge position on the Pd (211) step sites (Figure 2 (2B)). Xu et al. also reported the bridge position on stepped surface to be the preferred binding site for Cl atom[26]. This step is found to exothermic, having a reaction energy of -107 kJ/mol and an activation energy of 15 kJ/mol, which is slightly lower in comparison to the close-packed Pd (111) facet (E_a = 25 kJ/mol). Considering the more open Pd (100) facet, it is observed that two Cl atoms of the TCE molecule form bonds with the Pd surface (Figure 2 (3A)). This may be attributed to the distortion in the TCE geometry upon adsorption, in comparison to its gas-phase geometry. Dechlorination of TCE on Pd (100) is identical to that observed on Pd (111) and Pd (211). The C-Cl bond in cis-position to C-H bond stretches to 1.8 Å upon adsorption (Figure 2 (3A)). The activation energy for this dechlorination step is 14 kJ/mol, which is close to the value obtained on Pd (211) facet (E_a = 15 kJ/mol). At the transition state, the C-Cl bond elongates to 2.2 Å. The detached Cl atom finally occupies the hollow site, where it forms bonds with 4 surface Pd atoms and this corresponds well with the findings by Xu and co-workers[26] for Cl binding site on Pd (100) facet (Figure 2 (3B)). It is observed that, in the product state of the reaction intermediate, one of the Cl atoms, which is attached to the same C as H atom (marked as C_1 in Figure 1), makes a bond with the Pd surface (Figure 2 (3B)). However, the dechlorination step is observed to be different over the Pd (110) facet. On this surface, the adsorbed TCE molecule is highly distorted, leading to stretching of all three C-Cl bonds to a greater extent in comparison to the other three Pd facets, as shown in Figure 2 (4A). Owing to this configuration of the reactant state structure, two Cl atoms break simultaneously from the adsorbed TCE molecule leading to the formation of CH-CCl intermediate in a single step. Both these Cl atoms, after dissociation, make a bond with two surface

Pd atoms in a bridge configuration (Figure 2 (4C)). The activation energy for the simultaneous detachment of these two Cl atoms is 9 kJ/mol and this step is highly exothermic in nature (E_{rxn} = -138 kJ/mol). The CH-CCl intermediate makes a bond with the top Pd step sites in a bridge configuration (Figure 2 (4C)).
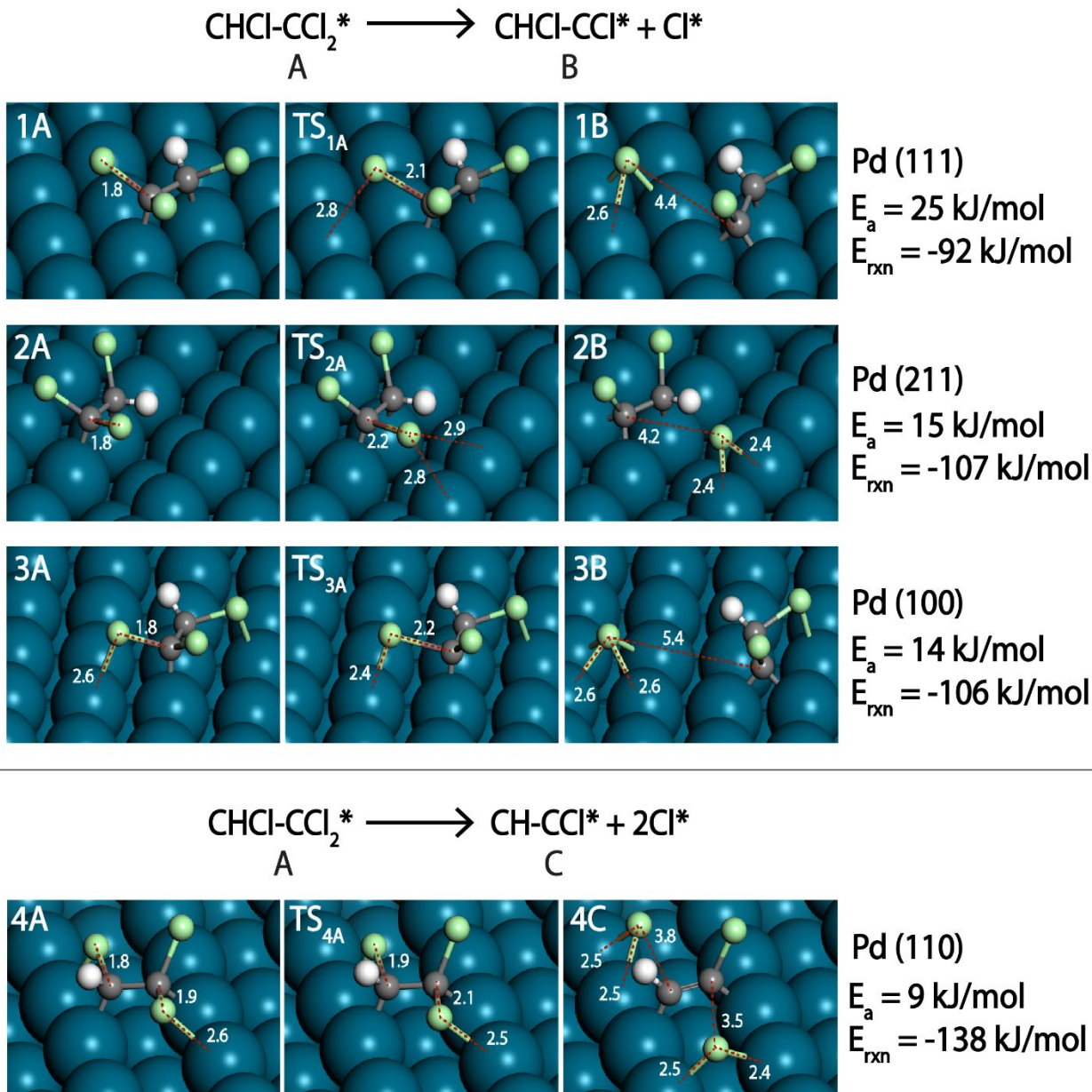

Figure 2. Reactant, transition and product state structures for the first dechlorination step on the Pd (111), Pd (211), Pd (100) and Pd (110) surfaces. The Pd atoms are displayed in blue, Cl atoms in green, C atoms in grey and H atom in white color. Distances are marked in Å.

The calculated activation energies for the hydrogenation of CHCl-CCl intermediate are high compared to the second dechlorination step (Table S1) on all the Pd surfaces and thus hydrogenation route is not considered. The second dechlorination step, as shown in Scheme 1, proceeds with CHCl-CCl intermediate as the reactant over Pd (111), Pd (211) and Pd (100). The C_1-Cl bond length (Figure 1) in the CHCl-CCl intermediate was calculated to be longer than the C_2-Cl bond length on the three Pd facets (Pd (111), Pd (211) and Pd (100)). Thus, in this dechlorination step, the C_1-Cl (Figure 1) bond dissociates over all three Pd surfaces as shown in Figure 3. DFT simulations show that on the Pd (111) facet, the C-Cl bond length increased from 1.8 Å in the reactant state (Figure 3 (1B)) to 2.3 Å in the transition state (Figure 3 (TS_{1B})) to 5.0 Å in the product state (Figure 3 (1C)). The activation energy for the second dechlorination step is calculated to be 16 kJ/mol on Pd (111). This value is slightly greater than the activation energy value of 8 kJ/mol, reported by Andersin et al., for the same step on Pd (111) surface[13]. However, for the same dechlorination step on the stepped Pd (211) surface, the activation energy is negligible ($E_a = 1$ kJ/mol), which is quite low compared to the Pd (111) facet ($E_a = 16$ kJ/mol). This suggests that the step sites aid in decreasing the barrier for C-Cl bond cleavage. An early transition state is observed on Pd (211), wherein the C-Cl bond stretched to 1.9 Å and simultaneously formed a bond with the Pd step site (Figure 3 (TS_{2B})). On Pd (100) facet, the Cl atom in the initial state also formed a bond with the Pd surface (Figure 3 (3B)). The C_1-Cl bond length of 1.9 Å is stretched to 2.4 Å at the transition state, where it shows a single bond with the Pd surface (bond length = 2.4 Å) (Figure 3 (TS_{3B})). In the final state of this dechlorination step, similar to the configurations observed on Pd (111) and Pd (211), both the C atoms bind to the same Pd atom, with each C atom also simultaneously making a bond with two other Pd atoms. The activation energy calculated for this step on Pd (100) ($E_a = 5$ kJ/mol) is similar to the one on Pd (211) surface ($E_a = 1$ kJ/mol) (Figure 3 (2B to 2C)) and is quite low compared to the Pd (111) facet ($E_a = 16$ kJ/mol) (Figure 3 (1B to 1C)). On comparing the first two steps involving Cl abstraction on Pd (111), Pd (211) and Pd (100) surfaces, it is observed that the barriers are comparatively lower for the second dechlorination step.

CHCl-CCl* $\longrightarrow$ CH-CCl* + Cl*
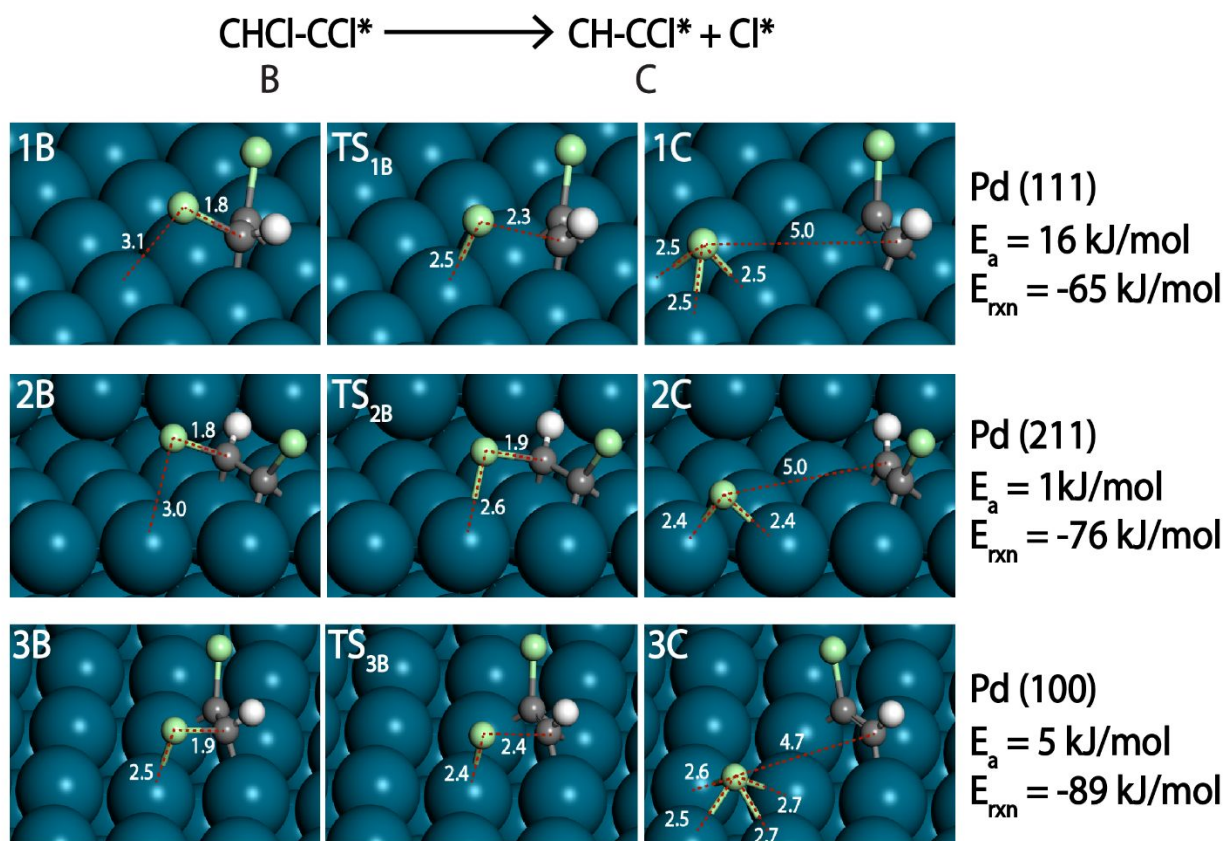B   C

Figure 3. Reactant, transition and product state structures for the second dechlorination step on the Pd (111), Pd (211) and Pd (100) surfaces. The Pd atoms are displayed in blue, Cl atoms in green, C atoms in grey and H atom in white color. Distances are marked in Å.

Following the dissociation of two Cl atoms, chloroacetylene (CH-CCl) is observed as a product intermediate on Pd (111), Pd (211), Pd (100) and Pd (110) surfaces. The hydrogenation barriers of CH-CCl are calculated to be much higher than further dechlorination barriers (Table S1), hence the dechlorination route is preferred. DFT simulations show that the dechlorination of chloroacetylene on all the Pd facets proceed with a relatively higher barrier, in comparison to the removal of the first two Cl atoms on the respective surfaces. Figure 4 displays the dechlorination step of CH-CCl leading to the formation of CH-C (ethynyl) intermediate on the different Pd facets. The activation energy on Pd (111) surface is calculated to be 52 kJ/mol (Figure 4 (1C to 1D)), which is almost double the value calculated for the first dechlorination step (25 kJ/mol) (Figure 2 (1A to 1B)). For the same step over Pd (111) surface, Andersin et al. reported a barrier of 53 kJ/mol, citing the initial orientation of C-Cl bond being directed away from the surface as the

probable reason for high barrier[13]. Compared to the Pd (111) surface, the activation energy for C-Cl bond dissociation on Pd (211) surface is calculated to be 29 kJ/mol. The C-Cl bond is observed to be pointing towards the Pd atom at the top step site in the initial state (Pd-Cl bond length = 3.3 Å) (Figure 4 (2C)) which stretches to 2.5 Å at the transition state, with the Cl atom forming a Pd-Cl bond (2.4 Å) as shown in Figure 4 (TS$_{2C}$). The final configuration of ethynyl intermediate (CH-C) as observed on Pd (111) facet and Pd (211) facet is found to be different, in which, on the former, each C atom occupies the hollow site (Figure 4 (1D)), whereas, on the latter, the C atom with no H atom occupies the hollow site and the C having H atom forms a bond with two Pd surface atoms. (Figure 4 (2D)). On the Pd (100) surface, the structure of the transition state is observed to be different. The C-Cl bond length elongates from 1.8 Å in the reactant state (Figure 4 (3C)) to 2.1 Å in the transition state but the Cl atom does not form any bond with the Pd surface (Figure 4 (TS$_{3C}$)). In the final state, the Cl atom occupies the hollow site on the Pd surface and the ethynyl intermediate also positions itself at the hollow site, with each C atom binding to two Pd atoms in a bridge position (Figure 4 (3D)). The dechlorination barrier for CH-CCl on the open Pd (100) surface is calculated to be 49 kJ/mol, which is close to the value calculated over Pd (111). This step is more exothermic on Pd (100) (E_{rxn} = -91 kJ/mol) compared to the Pd (111) facet (E_{rxn} = -30 kJ/mol) and signifies that the product state is more stable compared to the reactant state. Over the Pd (110) facet, the binding configuration of chloroacetylene is observed to be distinct from the other three Pd facets. In this, each C atom forms a single bond with the Pd atom, in a bridge position (Figure 4 (4C)). The C-Cl bond, initially at 1.8 Å (Figure 4 (4C)) stretches to 2.1 Å at the transition state, the Cl atom simultaneously making a bond with the Pd atom at the atop position (Figure 4 (TS$_{4C}$)) leading to differential stabilization of the transition state, which resulted in a lower activation energy (E_a = 36 kJ/mol). The ethynyl intermediate formed on Pd (110) (Figure 4 (4D)) surface shows a similar binding configuration as observed on the Pd (211) facet (Figure 4 (2D)). The Cl atom occupies the bridge position in its most stable configuration on the Pd (110) surface (Figure 4 (4D)). This step on the Pd (110) is found to be highly exothermic with a reaction energy of -182 kJ/mol, compared to the other three Pd facets – Pd (111) (E_{rxn} = -30 kJ/mol), Pd (211) (E_{rxn} = -49 kJ/mol) and Pd (100) (E_{rxn} = -91 kJ/mol), which suggests the high stability of the absorbed ethynyl intermediate on Pd (110) surface. Overall, from these calculations, it is observed that the Pd (211) and Pd (110) facets facilitate easy cleavage of C-Cl bond relative to the terrace Pd (111) and Pd (100) sites, owing to the comparatively higher activation energies on Pd (111)

and Pd (100) for dechlorination of chloroacetylene. The energy diagram for the three Cl abstractions is shown in Figure 5. To understand how well the transition state geometry scales with the geometry of the product state, transition state scaling relations[50,51] are plotted, as displayed in Figure 6, for the dechlorination steps on the Pd (111), Pd (211), Pd (100) and Pd (110) surfaces. It is observed that for the first and second dechlorination steps, the fit is linear. However, the third dechlorination step shows a reduced linear fit with a negative slope. This could be attributed to the change in the transition state configuration on different palladium facets relative to its product state configuration. In a study conducted by Ding and Maestri for the dissociation of trans-COOH catalyzed by different metals and different facets[52], a similar observation was made, wherein the Bronsted-Evans-Polanyi relations did not hold true.

CH-CCl* ⟶ CH-C* + Cl*

C   D

Pd (111)
E_a = 52 kJ/mol
E_{rxn} = -30 kJ/mol

Pd (211)
E_a = 29 kJ/mol
E_{rxn} = -49 kJ/mol

Pd (100)
E_a = 49 kJ/mol
E_{rxn} = -91 kJ/mol
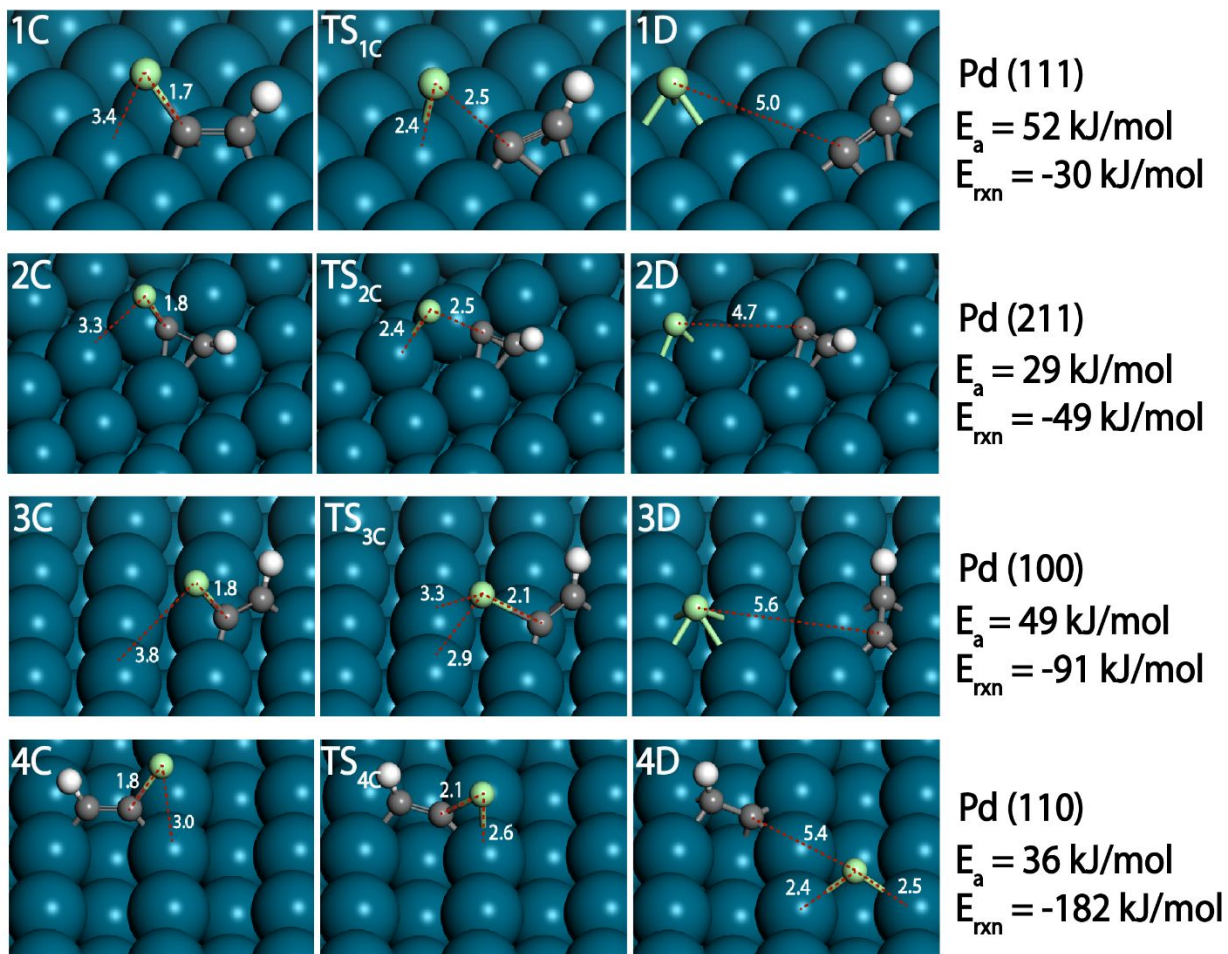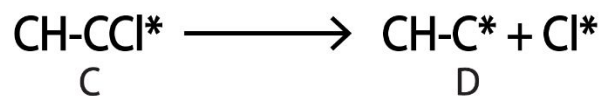
Pd (110)
E_a = 36 kJ/mol
E_{rxn} = -182 kJ/mol

Figure 4. Reactant, transition and product state structures for the third dechlorination step on the Pd (111), Pd (211), Pd (100) and Pd (110) surfaces. The Pd atoms are displayed in blue, Cl atoms in green, C atoms in grey and H atom in white color. Distances are marked in Å.
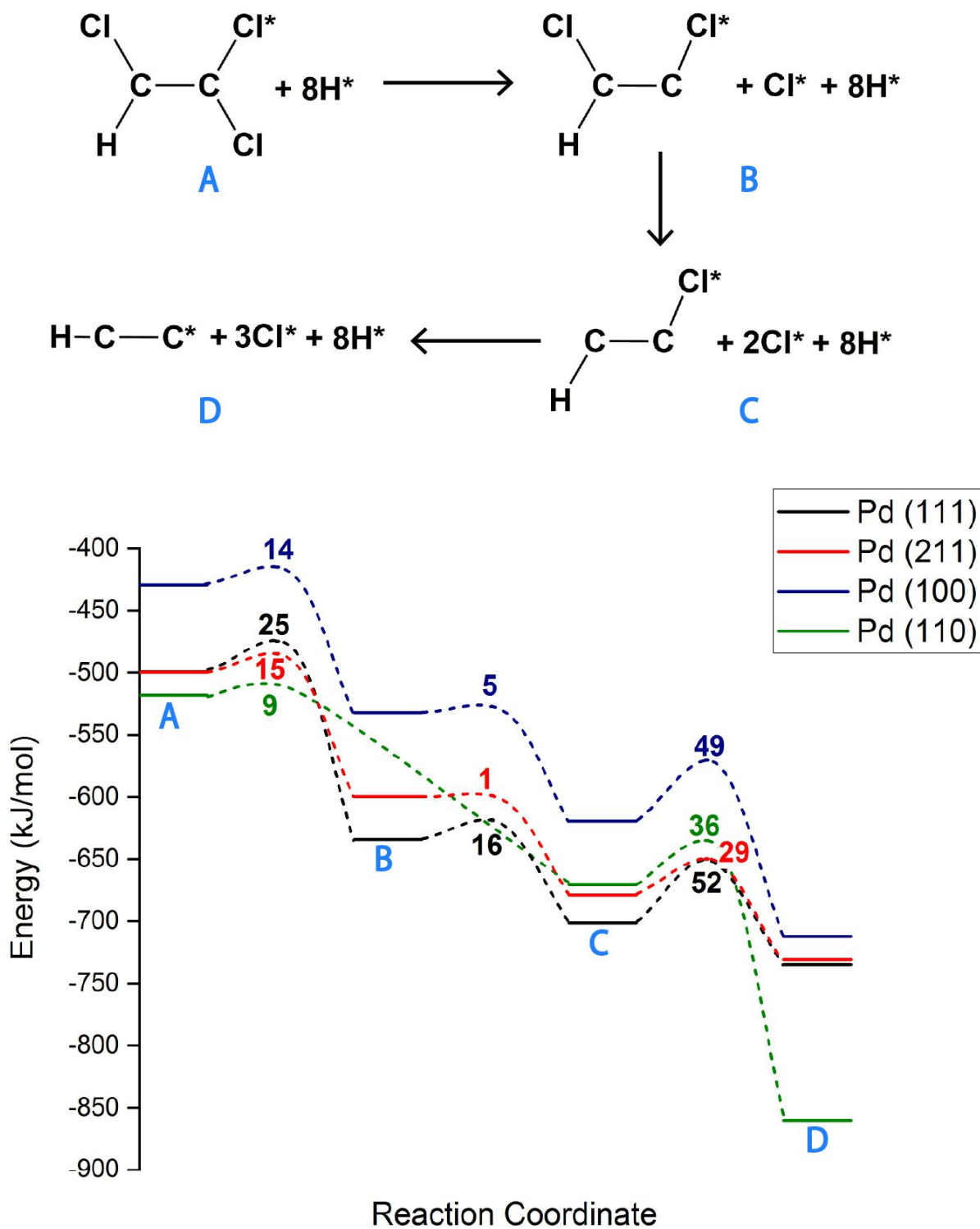
Figure 5. The energy diagram for the dechlorination steps in the HDC reaction of TCE on the Pd (111), Pd (211), Pd (100) and Pd (110) surfaces. Numbers in bold are showing the intrinsic activation energies of the elementary reaction steps in kJ/mol.
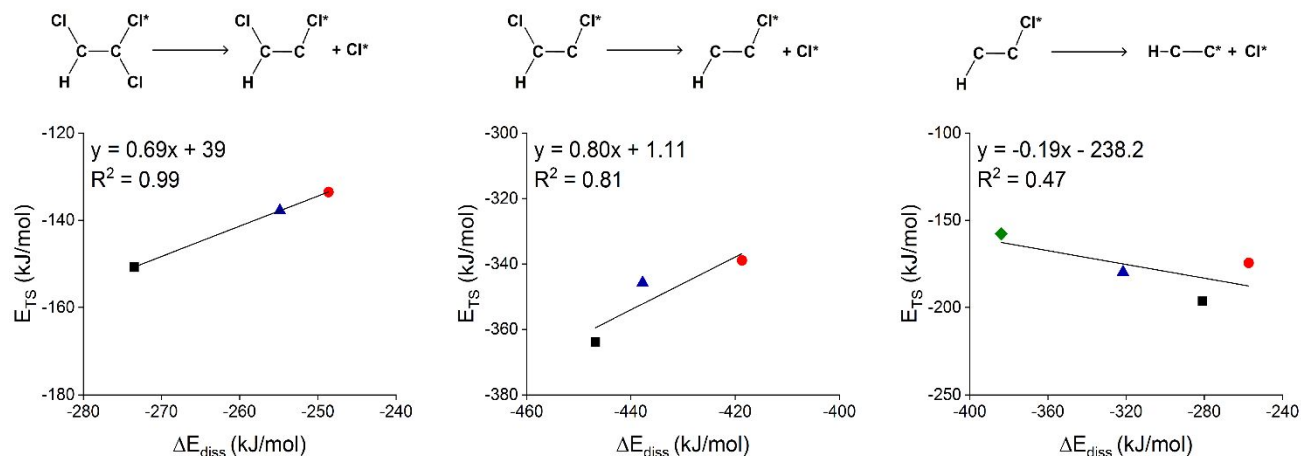
Figure 6. The transition state scaling relations obtained for the dechlorination steps of TCE on the Pd (111) (■), Pd (211) (●), Pd (100) (▲) and Pd (110) (◆) surfaces.

From our calculations, the barriers for all three chlorine abstractions are significantly low, specifically on the Pd (211) and Pd (110) surfaces (Figure 5). The pathway involving the addition of hydrogen to the intermediate chlorinated species (CHCl-CCl, CH-CCl) shows a higher barrier when compared with the subsequent dechlorination steps on all Pd facets (Table S1), hence is not considered further. Owing to this, complete dechlorination of TCE has been observed prior to hydrogenation of the intermediate hydrocarbon compound, which in this case is CH-C. Similar trends have been observed in the HDC of chloroform[26] and 1,1,1-trichloroethane[53], wherein hydrogenation followed complete dechlorination on the Pd surface. In the case of TCE HDC, ethynyl species (CH-C) is considered to be the precursor ahead of further hydrogenation as the barriers reported for C-C bond cleavage and C-H bond cleavage are very high on the terrace and step sites[15,54]. Therefore, on all the Pd facets, the first hydrogenation step progresses with the addition of H to the CH-C (ethynyl) intermediate. The pathways displaying lower barriers towards the formation of ethylene, in accordance with Scheme 1, are considered. Figure 7 displays the energy diagram for the hydrogenation route leading to ethane formation due to subsequent ethylene hydrogenation. Although ethylene could be a possible product, DFT calculations exhibit a lower activation energy for ethylene hydrogenation to ethyl species compared to the ethylene desorption energies on all the Pd facets (Table S2). Similar findings by Han and co-workers in an experimental study for the HDC of 1,2-dichloroethane wherein higher selectivity towards ethane has been

observed over the Pd/ZrO$_2$ catalyst[53]. Figures S3 to S8 display the elementary hydrogenation steps and the transition state scaling relations on different Pd surfaces.

Figure 7. The energy diagram for the hydrogenation steps in the HDC reaction of TCE on the Pd (111), Pd (211), Pd (100) and Pd (110) surfaces.

As a result of cleavage of C-Cl bonds prior to hydrogenation, chlorine atoms tend to accumulate on the Pd surface. Poisoning of the Pd surface due to Cl atoms has been observed at industrial scale which hinders its applicability as an industrial catalyst for the treatment of contaminants[11].

This Cl poisoning effect on Pd catalyst has also been reported in experimental studies for HDC reactions[12,55,56]. Moreover, the reaction intermediates tend to bind weakly to the surface in presence of chlorine[57].The desorption of atomic chlorine is stated to follow first-order kinetics with an activation energy of 174 ± 4 kJ/mol[58] on Pd (111) surface, with no desorption peaks observed for Cl_2. Tysoe and Lambert further elaborated that atomic chlorine desorbed at around 800 K under very low surface coverage conditions[58]. DFT calculations are therefore performed on clean Pd surfaces to understand the inhibitory effect of adsorbed chlorine. Figure 8 displays the most stable binding configurations of chlorine on the different Pd surfaces in their increasing order. The binding energy of chlorine is calculated to be the lowest over the Pd (111) facet (Figure 8 (a), B.E = -168 kJ/mol), followed by Pd (100) (Figure 8 (b), B.E = -178 kJ/mol) and Pd (211) (Figure 8 (c), B.E = -183 kJ/mol), which are almost comparable, and the highest binding energy is observed over Pd (110) surface (Figure 8 (d), B.E = -190 kJ/mol). Xu et al., by utilizing DFT simulations for HDC of chloroform on different Pd facets have also shown that chlorine binds strongly to the undercoordinated Pd surfaces (Pd (211) and Pd (100)) than the terrace Pd (111) surface[26] which corresponds well with our findings. These results suggest easy poisoning of nanoparticles that are smaller in size as they contain a lower fraction of terrace sites compared to large-sized nanoparticles.

Further, the formation of HCl aids in the removal of chlorine. Under ultra-high vacuum (UHV) conditions, it has been observed that cis-1,2-dichloroethylene decomposes on Pd (111), leading to the formation of HCl as a result of the combination of surface chlorine and hydrogen, above 420 K. Also, no peak corresponding to Cl_2 was observed[14] in the temperature-programmed desorption (TPD) studies. Hence, to gain mechanistic insights into the removal of Cl as HCl during HDC of TCE, DFT calculations are performed. Figure 9 shows the combination of adsorbed Cl atom and H atom to form gaseous HCl over the Pd (111), Pd (211), Pd (100) and Pd (110) facets. This step is observed to be endothermic and has a high barrier over all the Pd surfaces. Over the Pd (111) facet, both H and Cl atoms, initially at their most stable binding sites and 3.5 Å distance apart (Figure 9 (1J)), move towards each other at the transition state (Figure 9 (TS$_{1J}$)). The Cl atom changes its binding configuration to bridge position, with the distance from the H atom decreased to 1.8 Å (Figure 9 (TS$_{1J}$)). The activation energy for the formation of HCl over Pd (111) is calculated to be 90 kJ/mol and is endothermic in nature, with E_{rxn} = 78 kJ/mol (Figure 9 (1J to 1K)). Considering the HCl formation on Pd (211), it is observed that the transition state structure

on this stepped facet (Figure 9 (TS_{2J})) is quite analogous to the structure observed on Pd (111) (Figure 9 (TS_{1J})), with the exception of H and Cl atom being attached to the same step Pd atom and simultaneously forming a bond with each other. Although the H-Cl bond length on Pd (211) surface decreased to 1.5 Å at the transition state (Figure 9 (TS_{2J})), whereas on Pd (111), it is observed to be 1.8 Å (Figure 9 (TS_{1J})), the barrier for HCl formation on Pd (211) is relatively higher (E_a = 109 kJ/mol) compared to Pd (111). This could be ascribed to the higher binding energy of Cl on the Pd (211) surface (B.E = -183 kJ/mol, Figure 8 (c)) compared to the Pd (111) surface (B.E = -168 kJ/mol, Figure 8 (a)), which leads to higher activation energy on Pd (211) facet. The formation of hydrogen chloride is highly endothermic on the stepped facet (E_{rxn} = 103 kJ/mol) (Figure 9 (2J to 2K)). On Pd (100), the Cl atom initially occupies the four-fold hollow site (Figure 9 (3J)), which at the transition state, completely moves away from the Pd surface (Figure 9 (TS_{3J})). The transition state structure on Pd (100) is different compared to the Pd (111) and Pd (211) facets, wherein the H atom simultaneously makes a bond with Cl (H-Cl bond distance = 1.6 Å) and surface Pd atom (H-Pd bond distance = 1.7 Å) (Figure 9 (TS_{3J})). The barrier is calculated to be 88 kJ/mol which is close to the value observed on Pd (111). However, the activation energies are calculated to be higher on the step Pd (211) facet (Figure 9 (2J to 2K)) compared to the Pd (100) facet (Figure 9 (3J to 3K)), both surfaces having almost similar chlorine binding energies. This suggests that although chlorine has the ability to bind strongly to both Pd (100) and Pd (211) surfaces, it is easier to remove chlorine as HCl from the Pd (100) surface than the Pd (211) surface and therefore, can lead to deactivation of the step Pd (211) sites. Similarly, the activation energy for the formation of HCl on Pd (110) facet is calculated to be 118 kJ/mol (Figure 9 (4J to 4K)) and is higher than the Pd (211) facet by 9 kJ/mol. The high binding energy of chlorine on Pd (110) could possibly explain the reason for high activation energy, which corresponds well with the work conducted by Bloxham et al.[59] As shown in Figure 9 (4J), in the initial state, H occupies the hollow site and Cl is bound to top Pd atoms in a bridge configuration, both separated by a distance of 4.2 Å. The H and Cl atoms move towards each other and at the transition state (Figure 9 (TS_{4J})), the chlorine atom binds in an atop mode to the same Pd atom as hydrogen, the distance between them decreasing to 1.9 Å and finally they desorb as HCl (Figure 9 (4K)). The reaction energy for this step on Pd (110) is calculated to be 109 kJ/mol. The high endothermicity of HCl formation steps on the Pd (110) surface indicates the requirement of high reaction temperatures (390 K to 675 K[59]) for the removal of surface chlorine as HCl. The trends observed on the different Pd facets can also

be correlated with the metal dispersion, wherein for lower dispersion, large particle size are obtained[60]. As the size of the nanoparticle increases, the fraction of terrace site also increases[47]. Experimental work done by Diaz and co-workers employing various carbon supported Pd nanoparticles for aqueous phase HDC of TCE is observed to be structure sensitive[4]. The activity, however, is attributed to lower dispersion and larger particle size of Pd under the given reaction conditions (temperature = 303 K, pressure = 5 MPa), where Pd supported on activated carbon (having a particle size = 3 nm) reached 60% conversion after 180 minutes of reaction whereas Pd supported on high surface area graphite (having a particle size = 9 nm) reached 100% conversion in 60 minutes[4]. The increase in particle size may have diminished the inhibitory effect due to Cl, resulting in faster conversion of TCE on Pd supported on high surface area graphite. Similar findings on Cl poisoning for supported Pd catalysts have been reported by Aramendia et al. in the case of liquid phase HDC of chlorobenzene[55]. This observation could be attributed to the strong binding of chlorine on the step Pd (211) and corrugated Pd (110) sites, which then desorbs as HCl on reacting with surface hydrogen, with a very high activation energy, which is evident from this DFT study. In addition, bimetallic alloys may be rationally designed and synthesized to destabilize the chlorine binding on the catalyst surface[61–63]. The energy diagram for hydrogen chloride formation on different Pd facets is depicted in Figure S9.
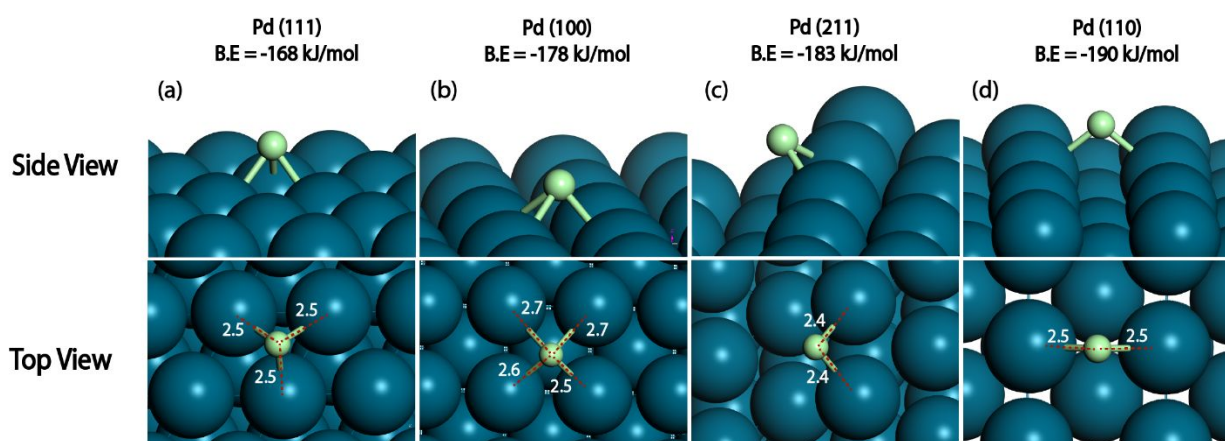

Figure 8. The most stable binding modes of chlorine on (a) Pd (111), (b) Pd (211), (c) Pd (100) and (d) Pd (110) surfaces. The Pd atoms are displayed in blue and Cl atoms in green color. Distances are marked in Å.
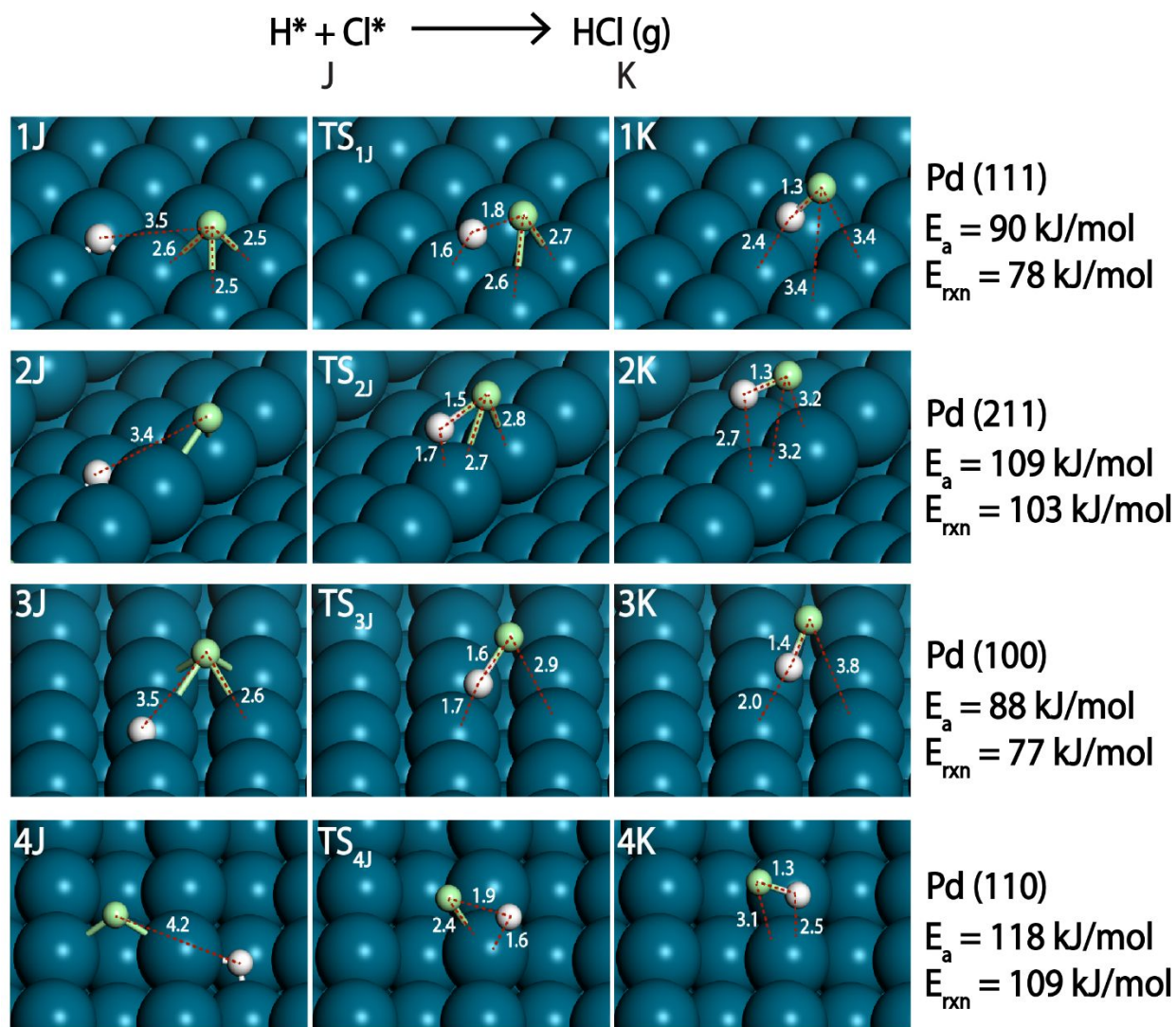
Figure 9. Reactant, transition and product state structures for the formation of HCl on the Pd (111), Pd (211), Pd (100) and Pd (110) surfaces. The Pd atoms are displayed in blue, Cl atoms in green and H atom in white color. Distances are marked in Å.

Conclusion:

On performing DFT simulations for the HDC reaction of TCE on different facets of the Pd catalyst, activation energies for the dechlorination steps of TCE are observed to be significantly lower as compared to the hydrogenation steps. TCE adsorption on Pd facets follows the trend: Pd (110) > Pd (100) > Pd (211) > Pd (111), which is in agreement with the d-band centers of the respective Pd facets. As compared to TCE, the binding energy of Cl atoms is calculated to be significantly higher on all the Pd facets. Thus, as observed in experiments, chlorine accumulates on the Pd

surface and impedes the activity of the catalyst. The formation of hydrogen chloride aids in the elimination of surface adsorbed Cl atoms. This step is calculated to be endothermic over all the Pd facets. The activation energies for this intrinsic step are calculated to be significantly higher on the undercoordinated Pd (211) and Pd (110) surfaces, indicating the difficulty in Cl removal on these facets as compared to the terrace sites (Pd (111) and Pd (100)). Thus, the DFT study agrees well with the experimental findings, wherein small sized Pd nanoparticles (higher fraction of step and corrugated sites) tend to display lower TCE conversions, in comparison to larger nanoparticles (higher fraction of terrace sites) during the HDC reaction. Consequently, this mechanistic understanding could provide a rationale for designing suitable catalysts having more terrace sites (large sized nanoparticles), thus reducing the effect of chlorine poisoning for the HDC reaction of TCE.

Acknowledgments

References:

1   S. Tabrez and M. Ahmad, *Toxicol. Environ. Chem.*, 2011, **93**, 73–84.

2   In *WHO Guidelines for Drinking-water Quality*, 2005.

3   *Guidelines for Drinking-water Quality, Fourth Edition*, 2011.

4   E. Diaz, L. Faba and S. Ordonez, *Appl. Catal. B Environ.*, 2011, **104**, 415–417.

5   M. G. Davie, H. Cheng, G. D. Hopkins, C. A. Lebron and M. Reinhard, *Environ. Sci. Technol.*, 2008, **42**, 8908–8915.

6   S. Kovenklioglu, Z. Cao, D. Shah, R. J. Farrauto and E. N. Balko, *AIChE J.*, 1992, **38**, 1003–1012.

7   C. G. Schreier and M. Reinhard, *Chemosphere*, 1995, **31**, 3475–3487.

8   B. P. Chaplin, M. Reinhard, W. F. Schneider, C. Schüth, J. R. Shapley, T. J. Strathmann and C. J. Werth, *Environ. Sci. Technol.*, 2012, **46**, 3655–3670.

9   G. V. Lowry and M. Reinhard, *Environ. Sci. Technol.*, 2000, **34**, 3217–3223.

10   F. J. Urbano and J. M. Marinas, *J. Mol. Catal. A Chem.*, 2001, **173**, 329–345.

11   S. Ordóñez, B. P. Vivas and F. V. Díez, *Appl. Catal. B Environ.*, 2010, **95**, 288–296.

12   K. N. Heck, M. O. Nutt, P. Alvarez and M. S. Wong, *J. Catal.*, 2009, **267**, 97–104.

13   J. Andersin, P. Parkkinen and K. Honkala, *J. Catal.*, 2012, **290**, 118–125.

14   D. M. Jaramillo, D. E. Hunka and D. P. Land, *Langmuir*, 2004, **20**, 5782–5785.

15   Z. X. Chen, H. A. Aleksandrov, D. Basaran and N. Rösch, *J. Phys. Chem. C*, 2010, **114**, 17683–17692.

16   M. Neurock and R. A. Van Santen, *J. Phys. Chem. B*, 2000, **104**, 11127–11145.

17   H. A. Aleksandrov, L. V. Moskaleva, Z. J. Zhao, D. Basaran, Z. X. Chen, D. Mei and N. Rösch, *J. Catal.*, 2012, **285**, 187–195.

18   A. Kausamo, J. Andersin and K. Honkala, *J. Phys. Chem. C*, 2014, **118**, 19759–19767.

19   J. Andersin and K. Honkala, *Phys. Chem. Chem. Phys.*, 2011, **13**, 1386–1394.

20   G. Porwal, S. Gupta, S. Sreedhala, J. Elizabeth, T. S. Khan, M. A. Haider and C. P. Vinod, *ACS Sustain. Chem. Eng.*, 2019, **7**, 17126–17136.

21   F. Jalid, T. S. Khan and M. A. Haider, *Catal. Sci. Technol.*, 2021, **11**, 97–115.

22   F. Jalid, M. A. Haider, M. I. Alam and T. S. Khan, *Catal. Sci. Technol.*, 2021, **11**, 2130–2143.

23   S. Gupta, M. I. Alam, T. S. Khan and M. A. Haider, *ACS Sustain. Chem. Eng.*, 2019, **7**, 10165–10181.

24   G. C. Bond, *Surf. Sci.*, 1985, **156**, 966–981.

25   D. Shuai, D. C. McCalman, J. K. Choe, J. R. Shapley, W. F. Schneider and C. J. Werth, *ACS Catal.*, 2013, **3**, 453–463.

26   L. Xu, S. Bhandari, J. Chen, J. Glasgow and M. Mavrikakis, *Top. Catal.*, 2020, **63**, 762–776.

27   A. R. Poerwoprajitno, L. Gloag, S. Cheong, J. J. Gooding and R. D. Tilley, *Nanoscale*, 2019, **11**, 18995–19011.

28   S. Gupta, T. S. Khan, B. Saha and M. A. Haider, *Ind. Eng. Chem. Res.*, 2019, **58**, 16153–16163.

29   G. Kresse and J. Furthmüller, *Comput. Mater. Sci.*, 1996, **6**, 15–50.

30   T. S. Khan, S. Gupta, P. Bandodkar, M. I. Alam and M. A. Haider, *Appl. Catal. A, Gen.*, 2018, **560**, 66–72.

31   F. Jalid, T. S. Khan and M. A. Haider, *Catal. Today*, 2021, **370**, 151–160.

32   F. Jalid, M. A. Haider, M. I. Alam and T. S. Khan, *Catal. Sci. Technol.*, 2021, **11**, 2130–2143.

33   D. Vanderbilt, *Phys. Rev. B - Condens. Matter Mater. Phys.*, 1990, **41**, 7892–7895.

34   S. Grimme, J. Antony, S. Ehrlich and H. Krieg, *J. Chem. Phys.*, , DOI:10.1063/1.3382344.

35   H. J. Monkhorst and J. D. Pack, *Phys. Rev. B*, 1976, **13**, 5188–5192.

36   G. Henkelman and H. Jónsson, *J. Chem. Phys.*, 2000, **113**, 9978–9985.

37   G. Henkelman, B. P. Uberuaga and H. Jónsson, *J. Chem. Phys.*, 2000, **113**, 9901–9904.

38   J. W. Bozzelli, Y. Chen and C. Steven, *Chem. Eng. Commun.*, 1992, **115**, 1–11.

39   S. Ordóñez, H. Sastre and F. V. Díez, *Appl. Catal. B Environ.*, 2000, **25**, 49–58.

40   B. T. Meshesha, N. Barrabés, J. Llorca, A. Dafinov, F. Medina and K. Föttinger, *Appl. Catal. A Gen.*, 2013, **453**, 130–141.

41   A. Śrebowata, K. Tarach, V. Girman and K. Góra-Marek, *Appl. Catal. B Environ.*, 2016, **181**, 550–560.

42   N. Barrabés, K. Föttinger, J. Llorca, A. Dafinov, F. Medina, J. Sá, C. Hardacre and G. Rupprechter, *J. Phys. Chem. C*, 2010, **114**, 17675–17682.

43   G. V. Lowry and M. Reinhard, *Environ. Sci. Technol.*, 1999, **33**, 1905–1910.

44   S. Li, Y. L. Fang, C. D. Romanczuk, Z. Jin, T. Li and M. S. Wong, *Appl. Catal. B Environ.*, 2012, **125**, 95–102.

45   S. Cao, F. F. Tao, Y. Tang, Y. Li and J. Yu, *Chem. Soc. Rev.*, 2016, **45**, 4747–4765.

46   M. Che and C. O. Bennett, *Adv. Catal.*, 1989, **36**, 55–172.

47   Q. Zhang, W. Deng and Y. Wang, *Chem. Commun.*, 2011, **47**, 9275–9292.

48   F. Mittendorfer, N. Seriani, O. Dubay and G. Kresse, *Phys. Rev. B - Condens. Matter Mater. Phys.*, 2007, **76**, 233413.

49   K. Mackenzie, H. Frenzel and F. D. Kopinke, *Appl. Catal. B Environ.*, 2006, **63**, 161–167.

50   S. Wang, V. Petzold, V. Tripkovic, J. Kleis, J. G. Howalt, E. Skúlason, E. M. Fernández, B. Hvolbæk, G. Jones, A. Toftelund, H. Falsig, M. Björketun, F. Studt, F. Abild-Pedersen, J. Rossmeisl, J. K. Nørskov and T. Bligaard, *Phys. Chem. Chem. Phys.*, 2011, **13**, 20760–

20765.

51   S. Wang, B. Temel, J. Shen, G. Jones, L. C. Grabow, F. Studt, T. Bligaard, F. Abild-Pedersen, C. H. Christensen and J. K. Nørskov, *Catal. Letters*, 2011, **141**, 370–373.

52   Z. Bin Ding and M. Maestri, *Ind. Eng. Chem. Res.*, 2019, **58**, 9864–9874.

53   Y. Han, J. Sun, H. Fu, X. Qu, H. Wan, Z. Xu and S. Zheng, *Appl. Catal. A Gen.*, 2016, **519**, 1–6.

54   J. Andersin and Honka, *Surf. Sci.*, 2010, **604**, 762–769.

55   M. A. Aramendia, V. Borau, I. M. Garcia, C. Jimenez, F. Lafont, A. Marinas, J. M. Marinas and F. J. Urbano, *J. Catal.*, 1999, **187**, 392–399.

56   E. Lopez, S. Ordóñez and F. V Diez, *Appl. Catal. B Environ.*, 2006, **62**, 57–65.

57   L. Xu, E. E. Stangland and M. Mavrikakis, *Catal. Sci. Technol.*, 2018, **8**, 1555–1563.

58   W. T. Tysoe and R. M. Lambert, *Surf. Sci.*, 1988, **199**, 1–12.

59   L. H. Bloxham, S. Haq, C. Mitchell and R. Raval, *Surf. Sci.*, 2001, **489**, 1–19.

60   O. L. Pérez, D. Romeu and M. J. Yacamán, *J. Catal.*, 1983, **79**, 240–241.

61   M. Gupta, T. S. Khan, S. Gupta, M. I. Alam, M. Agarwal and M. A. Haider, *J. Catal.*, 2017, **352**, 542–556.

62   T. S. Khan, F. Jalid and M. A. Haider, *Top. Catal.*, 2018, **61**, 1820–1831.

63   F. Jalid, T. S. Khan, F. Q. Mir and M. A. Haider, *J. Catal.*, 2017, **353**, 265–273.